



Regulating spin state of Fe active sites by the P-doping strategy for enhancing peroxymonosulfate activation

Zhaoyi Yang^{a,b}, Xiaofang Yang^a, Guangyu An^{c,d,*}, Dongsheng Wang^{e,**}

^a State Key Laboratory of Environment Aquatic Chemistry, Research Center for Eco-Environmental Sciences, Chinese Academy of Sciences, Beijing 100085, China

^b University of Chinese Academy of Science, Beijing 100049, China

^c Key Laboratory of Drinking Water Science and Technology, Research Center for Eco-Environmental Sciences, Chinese Academy of Sciences, Beijing 100085, China

^d National Engineering Research Center of Industrial Wastewater Detoxication and Resource Recovery, Beijing 100085, China

^e Department of Environmental Engineering, Zhejiang University, Hangzhou 310058, Zhejiang, China

ARTICLE INFO

Keywords:

P-doped

Electronic structure

Spin state

Electron transfer

PMS activation

ABSTRACT

Optimization of Fe-based heterogeneous catalyst for enhancing PMS activation was studied by an electronic structure regulation strategy. The single atom and nano-particle Fe-catalysts were then modified by P-doping on carbon support and tested for BPA degradation. Catalysts with P-doping led to 100 % BPA degradation in 30 min, much better than single atom and nano-particle control groups (56 % and 61 %). Experimental and DFT results revealed that P-doping increased the electron density of Fe and induced the transformation of Fe 3d electron spin state from low spin to medium spin, then the Fe 3d orbitals with high energy could better overlap with O 2p orbitals of PMS, promoting the electron transfer process from Fe to PMS and generation of hydroxyl radical. This work provides a deep understanding of spin state modulation for designing high-performance PMS activation catalysts.

1. Introduction

The shortage of clean water caused by persistent and refractory organic compounds resulting from rapid industrialization and urbanization has become one of the most serious restrictions for sustainable development of the world [1,2]. Therefore, it is crucial to develop efficient, economical and environmentally friendly technologies on the removal of refractory organics [3]. Among multitudinous technologies, heterogeneous peroxymonosulfate-based advanced oxidation processes (PMS-AOPs) have attracted great attention due to their high oxidation capability resulting from the produced reactive oxygen species (ROS) for degrading refractory organics, with the advantages of high oxidant mass density, easy transportation and storage, and catalyst recycling [4–8]. However, several potential problems limit the application of PMS-AOPs technology, such as (1) slow kinetics of adsorption/activation of PMS on catalytic active sites [9,10]; (2) low PMS utilization efficiency caused by the generation of low active species [11]; (3) self-quenching of active species and low mass transfer efficiency in aqueous solution, which seriously lower the utilization rate of PMS and overall oxidation efficacy

[12,13]. Therefore, it is essential to get a deep understanding on the microscopic structure-activity relationship for PMS activation in order to improve the performance of solid catalysts and further design the practical materials for PMS-AOPs techniques.

As one of the most abundant elements in the earth, Fe is widely used for developing new catalyst materials in PMS-AOPs studies for its high catalytic activity and environmentally friendly features [14,15]. To enhance the catalytic efficiency and atom utilization, researchers have made tremendous efforts to decrease the size of metal-based catalysts from micrometer to nanometer, then up to single-atom catalysts (SACs) [16–18]. Among the microminiaturization process of catalysts, the attention of scientists mostly focused on the size effect of target materials, which were relatively clear from theoretical level. In the field of PMS-AOPs, however, less research has been conducted on improving the catalytic efficiency from atomic level by modulating the intrinsic property of metal centers, which is the fundamental strategy to achieve the breakthrough for the catalytic activity of Fe-based catalysts. Recent studies have shown that modulating the electronic structure of metal centers is an effective method to improve the intrinsic catalytic activity

* Corresponding author at: Key Laboratory of Drinking Water Science and Technology, Research Center for Eco-Environmental Sciences, Chinese Academy of Sciences, Beijing 100085, China.

** Corresponding author.

E-mail addresses: gyan@rcees.ac.cn (G. An), wongds@zju.edu.cn (D. Wang).

<https://doi.org/10.1016/j.apcatb.2023.122618>

Received 20 December 2022; Received in revised form 6 March 2023; Accepted 11 March 2023

Available online 17 March 2023

0926-3373/© 2023 Elsevier B.V. All rights reserved.

for the oxygen-containing compound catalytic reactions [19]. Since the 3d orbitals can split into t_{2g} bonding orbitals and e_g antibonding orbitals under the influence of coordination field, the filling of 3d electrons will result various spin states, such as low spin (LS), medium spin (MS), and high spin (HS) states. The spin state type is determined by the number of 3d electrons and the energy difference between e_g and t_{2g} orbitals, which can be modulated by the chemical environment surrounding the metal centers. With regard to Fe, the LS state generally owns less unpaired electrons than the HS state. The HS state allows Fe to strongly interact with intermediates due to the excessive orbital overlap, which hinders the desorption of reactants and leads to the deterioration of catalytic performance [20]. In contrast, the MS state Fe is more likely to interact with the intermediates in the form of σ -bonds, which is beneficial to the both adsorption of the reactants and desorption of the products [21,22]. Therefore, for the reactions such as oxygen reduction (ORR), CO₂ reduction (CO₂RR), oxygen evolution reduction (OER) and water splitting reactions, the spin state has been gradually recognized as an important evaluation index for catalytic property, which is crucial in governing the adsorption strength of the intermediates on catalyst surface and dominating the surface redox kinetics [23–27]. However, so far, there are few studies reported in the field of PMS-AOPs to enhance catalytic performance by modulating the spin state of the metal center.

Regulation of the coordination environment by doping metallic or nonmetallic elements can effectively modulate the electronic structure of the metal center. It was reported that introducing Fe into ZnMn₂O₄ nanoparticles could induce the super-exchange interaction between Fe and Mn, causing high local delocalization of Mn-O and promoting the activation of PMS [28]. Besides that, introduction of non-metallic heteroatoms (B or P) into monometallic (Fe or Cu) carbon-based materials was also adopted to modulate the electronic structure by changing electron density of the metal center [29,30]. The above strategy was realized to optimize the adsorption of PMS and reduce the formation energy barrier of the hydroxyl radical (\bullet OH) by long-range interaction between metal centers and doped elements (located in the second coordination shell layer). Since the metal atom could be modified more effectively by modulating its first coordination shell layer, it is feasible to fine-tune the electronic structure by adjusting the 3d electron in order to achieve a more powerful regulating effect.

In this study, the Fe-based SACs and nanoparticles were employed as model catalysts to investigate the effect of P-doping on PMS activation. Since N-rich carbon materials can improve the stability and catalytic performance of small-sized metal catalysts due to N coordination reaction and high electron transfer capacity [31–35], ZIF-8 was applied as support precursor to load target Fe catalysts by in-situ synthesis. P element was introduced to form the “Fe-P” structure via coordination reaction and confinement effect, in order to directly regulate the electronic structure of Fe center. Bisphenol A (BPA) was used as the pollutant to evaluate the catalytic performance. Combining the experiments and density functional theory (DFT) calculations, the mechanism of P-induced spin state transformation and charge transfer toward PMS activation was proposed. The purpose was to reveal the general law of P-doping effect on electronic structure (spin state) modulation for Fe catalysts at different particle sizes.

2. Materials and methods

2.1. Materials

Iron nitrate nonahydrate (Fe(NO₃)₃·0.9 H₂O), zinc nitrate hexahydrate (Zn(NO₃)₂·0.6 H₂O), 2-methylimidazole and triphenylphosphine (PPh₃) were purchase from Aladdin. Potassium peroxydisulfate (PMS, KHSO₅·0.5KHSO₄·0.5 K₂SO₄), 5,5-dimethyl-1-pyrroline-N-oxide (DMPO), 2,2,6,6-tetramethyl-4-piperidinyloxy (TEMP), L-histidine, humic acid (HA), *p*-benzoquinone (BQ), Methyl alcohol (MeOH), tert-butanol (TBA, AR) were purchase from Sinopharm Chemical. Bisphenol (BPA), sulfamethoxazole (SMX), ibuprofen (IBP), carbamazepine

(CBZ), benzoic acid (BA), nitrobenzene (NB), methyl phenyl sulfoxide (PMSO), and methyl phenyl sulfone (PMSO₂) were obtained from Sigma. All chemicals were used as received without further purification. Deionized (DI) water with a resistivity of 18.2 MΩ cm⁻¹ was used throughout the experiments.

2.2. Synthesis of catalysts

The P-modified catalysts were prepared by an in-situ phosphatizing strategy combined with chemical and pyrolysis processes. As shown in Fig. 1a, ZIF-8 was in-situ self-assembled as the support precursor with a three-dimensional ordered pore structure. Due to the strong coordination reaction between Fe³⁺ and N, Fe atoms were anchored and dispersed on the pore surface of ZIF-8 and served as the metal source of single atoms (SAs) and nanoparticles (NPs). To dope P in the catalysts, triphenyl phosphorus (PPh₃) was used, as its molecular size (8.9 Å) was between the cage size (11.6 Å) and cage window (3.4 Å) of ZIF-8, so that PPh₃ could be effectively encapsulated in the cage and combined with Fe atoms. Then, the P-doped Fe SAs and NPs catalysts loaded on the N-containing carbon (NC) support were obtained by the pyrolysis treatment. By controlling the dosage of Fe salts, N, P-coordinated single-atom catalysts (Fe-SAs/PNC) and Fe_xP nanoparticles catalysts (Fe_xP-NPs/NC) were prepared. In addition, the control group catalysts were also prepared without P-doping and named as Fe-SAs/NC and Fe-NPs/NC, respectively. The blank sample NC was also prepared (without the addition of Fe and PPh₃). The detailed synthesis and characterization methods were shown in the [Supplementary Data](#).

2.3. Degradation experiments

The performance of the catalysts for peroxydisulfate (PMS) activation were evaluated by BPA degradation. Typically, 5.0 mg of catalysts was added to a 50 mL BPA solution (BPA = 10 mg L⁻¹, initial pH = 6.7). Then, the solution was stirred for 30 min to reach adsorption-desorption equilibrium. After this, the calculated PMS aqueous solution was added to initiate the test. During each time interval, 0.75 mL of the reaction solution was collected and injected into a vial containing 0.75 mL of methanol to terminate the catalytic reaction. The mixed suspension full shocked for 1 min, and then, it was filtered through a 0.22 μm Millipore film. The concentration of BPA was detected by a high-performance liquid chromatography (HPLC, Shimadzu LC-2010AHT) with a C-18 column. In the degradation experiment, the influences of various anions (Cl⁻, HCO₃⁻, H₂PO₄⁻, NO₃⁻) and humic acid were also investigated. As for the stability experiment, the spent catalyst was collected and washed with deionized water and methanol. After the vacuum drying at 70 °C for 12 h, it was then used for the next cycle. Besides, the catalytic performance of Fe-SAs/PNC for other organic pollutants were also conducted.

3. Results and discussions

3.1. Characterization of catalysts

The XRD results (Fig. S4) show that the Fe-based NPs were produced in Fe_xP-NPs/NC and Fe-NPs/NC, while Fe should be well dispersed in the form of SAs in Fe-SAs/PNC and Fe-SAs/NC. The compositions of the NPs in Fe₂P-NPs/NC and Fe-NPs/NC are determined as Fe₂P and Fe nanocrystals according to their characteristic peaks. To further confirm the Fe species, four catalysts were characterized by spherical aberration-corrected annular dark-field scanning transmission electron microscopy (AC HAADF-STEM). As shown in Fig. 1b–e, the target NPs and SAs catalysts were successfully prepared, where the NPs of 1–2 nm appeared in the Fe₂P-NPs/NC and Fe-NPs/NC samples, while only monodispersed single atoms (bright spots) were observed in the Fe-SAs/PNC and Fe-SAs/NC samples. Furthermore, by integrating the signal intensity along the X-Y axis (marked in Fig. 1d), the distance between

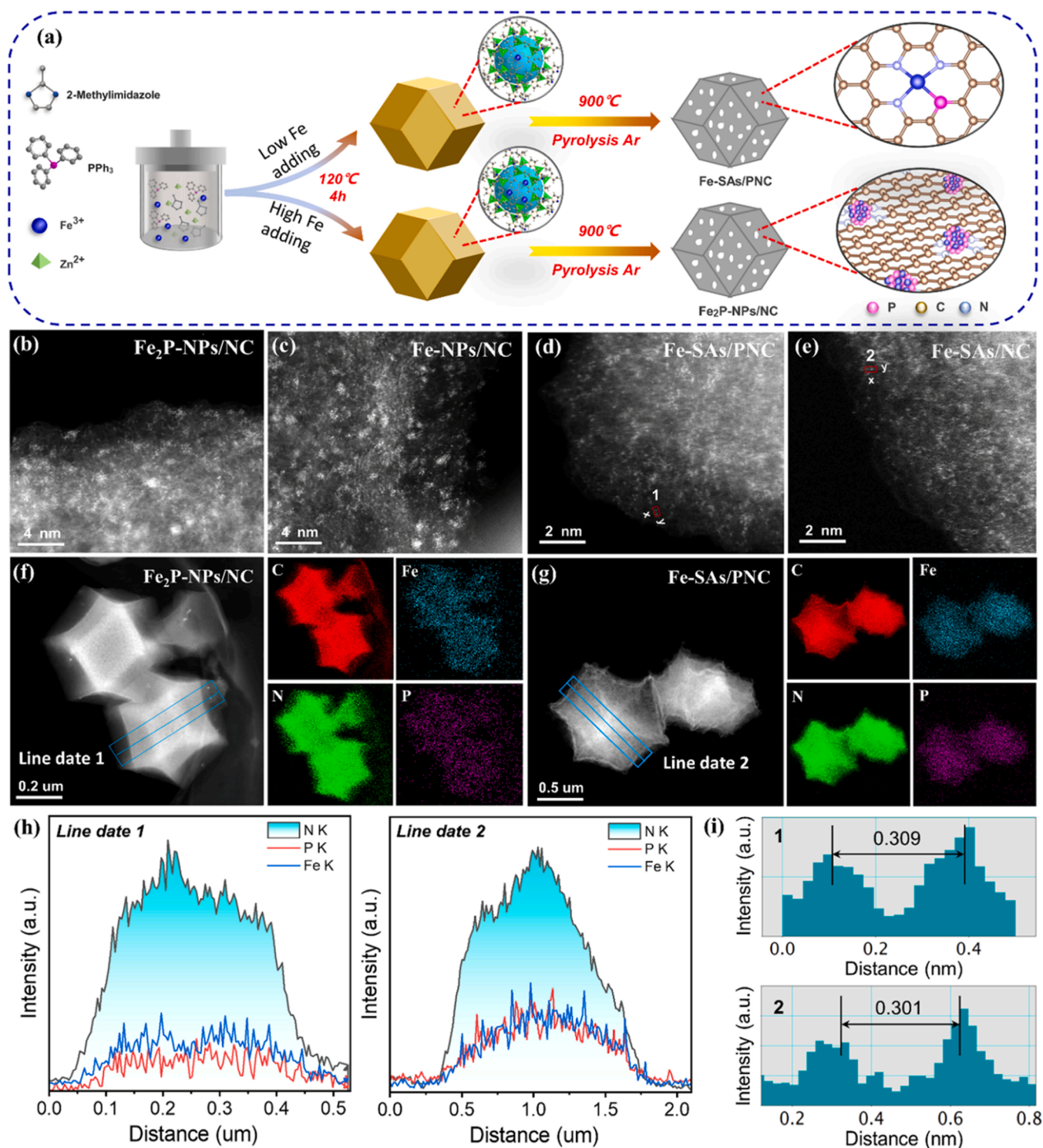


Fig. 1. (a) Schematic synthesis process of Fe-SAs/PNC and Fe₂P-NPs/NC. AC HADDF-STEM images of (b) Fe₂P-NPs/NC, (c) Fe-NPs/NC, (d) Fe-SAs/PNC, and (e) Fe-SAs/NC. HADDF-STEM and EDS mapping images of (f) Fe₂P-NPs/NC and (g) Fe-SAs/PNC. (h) The EDS line scanning data 1 and 2 in (f) and (g). (i) The corresponding intensity profiles obtained in area labels 1 and 2 in (d) and (e).

the close bright spots was determined as 0.309 nm, which was larger than the effective atomic diameter of Fe atom (0.248 nm) (Fig. 1i-1). The similar distance of 0.301 nm between two close bright spots was also obtained for Fe-SAs/NC (Fig. 1i-2). This result indicates that the Fe elements were distributed in Fe-SAs/PNC and Fe-SAs/NC samples by means of monodispersed single atoms. Energy dispersive analysis (EDS) results (Fig. 1f, 1g and Fig. S5) indicate that the Fe, N, or P elements were uniformly distributed in Fe₂P-NPs/NC, Fe-SAs/PNC, Fe-SAs/NC

and Fe-NPs/NC samples. In addition, the signal intensity of Fe element in Fe₂P-NPs/NC is slightly higher than that of P element compared to Fe-SAs/PNC (Fig. 1h), indicating that more Fe atoms agglomerated in Fe₂P NPs.

To analyze the structure of carbon supports, Raman spectroscopy was adopted to investigate the composition and defect situation of the catalysts. As shown in Fig. S6, two characteristic peaks of D-band for amorphous carbon ($\sim 1360\text{ cm}^{-1}$) and G-band for sp² carbon atom

($\sim 1580\text{ cm}^{-1}$) are present in the spectra for all catalysts, indicating that the supports are mainly composed of graphitized carbon with abundant defects. The broad 2D band at the Raman frequency shift of 2780 cm^{-1} also confirms this conclusion. The relative intensity ratio (I_D/I_G) of the D-band to G-band regularly increases with the doping of Fe and P elements. As the larger I_D/I_G value signifies the presence of more defect sites, it can be concluded that the introduced Fe and P atoms replaced the carbon atoms and firmly occupied the current sites, inducing the formation of defects and disordered graphitic structure. The specific area and pore size distribution were also characterized (Fig. S7 and Table S1). Compared to NC, the adsorption/desorption curves of four catalysts all exhibit noticeable hysteresis loops. In general, the pore sizes of four catalysts all increased compared to NC, while the specific area and pore volume values decreased on the contrary. This phenomenon might be induced by the partial fusion of the pores during the pyrolysis process after introduction of Fe and P. However, the three-dimensional ordered pore structures were preserved so that the Fe SAs and NPs could be well stably dispersed on the surface of the pore and interacted with oxidants and organic molecules by effective mass transfer in the pore passage.

To get an insight into the local chemical environment information of Fe atoms, the Fe K-edge X-ray near-edge absorption (XANES) technique was applied for all catalysts. As shown in Fig. 2a, the absorption edges of four catalysts are all located between the lines of Fe foil and Fe_2O_3 , implying that the mean valences of Fe lie in the range of 0–3. The absorption edge of Fe-SAs/PNC shift to the direction of low energy compared to Fe-SAs/NC, suggesting that the introduction of P lowered the oxidation state of Fe (calculated valence 2.3) (Fig. S8). The extended X-ray absorption fine structure (EXAFS) results were further obtained by Fourier transform of the K-edge XANES data. As shown in Fig. 2b, the R space of Fe-SAs/PNC and Fe-SAs/NC present a broad peak at 1.52 \AA and a narrow peak at 1.50 \AA , respectively, indicating that the Fe atoms in two catalysts are coordinated by N or P atoms in the first coordination shell [36,37]. Compared to Fe foil, there is no “Fe-Fe” peak ($R > 2.1\text{ \AA}$) appearing in the results of Fe-SAs/PNC and Fe-SAs/NC, which strongly

demonstrates that the Fe element in two catalysts is existing in the form of SAs. As shown in Fig. 2d, Fe-SAs/PNC presents the maximal value at 4.2 \AA^{-1} , which is near the Wavelet transform (WT) analysis results of FePc ($\sim 3.9\text{ \AA}^{-1}$), suggesting that Fe-SAs/PNC may contain the similar Fe coordination configuration to FePc. The least squares method was then used to fit the EXAFS curves. As shown in Table S2 and Fig. 2c, the broad peak at 1.52 \AA is fitted by Fe-N and Fe-P peaks, where the bond lengths of Fe-N and Fe-P are $1.90 \pm 0.05\text{ \AA}$ and $2.26 \pm 0.04\text{ \AA}$ and the coordination numbers are 3.4 ± 0.4 and 0.9 ± 0.3 , respectively. These results reveal that the coordination structure of the Fe-SAs/PNC is $\text{Fe-P}_1\text{N}_3$. Similarly, the Fe coordination structure in Fe-SAs/NC can be identified as Fe-N_4 according to Table S2 and Fig. 2e. For $\text{Fe}_2\text{P-NPs/NC}$ and Fe-NPs/NC , there are clear peaks appearing at 2.63 \AA and 2.12 \AA , respectively (Fig. 2b). In addition, the R space of $\text{Fe}_2\text{P-NPs/NC}$ also shows a strong peak at 1.72 \AA similar to Fe_2P , further confirming that the Fe_2P NPs was generated in the pyrolysis process. Moreover, the fitting analysis was also performed for the $\text{Fe}_2\text{P-NPs/NC}$ and Fe-NPs/NC (Table S2). The results confirm that the $\text{Fe}_2\text{P-NPs}$ and Fe-NPs were generated and connected to the carbon supports through Fe-P and/or Fe-N bonds for two catalysts.

3.2. Catalytic performance

As shown in Fig. 3a, $\text{Fe}_2\text{P-NPs/NC}$ and Fe-SAs/PNC behaved much better BPA degradation capacities, where 100 % of BPA were decomposed within 30 min, while only 61 % and 56 % BPA were degraded for Fe-NPs/NC and Fe-SAs/NC. In addition, $\text{Fe}_2\text{P-NPs/NC}$ and Fe-SAs/PNC also performed strong organic matter removal capacities with TOC removal rates over 70%, which were higher than those of Fe-NPs/NC and Fe-SAs/NC ($< 40\%$) (Fig. S10). To evaluate the real catalytic efficiency of Fe active sites, TOF_{Fe} was set and calculated as following: the BPA pseudo-first-order apparent rate constant (k_{obs}) divided by the amount of Fe atoms for catalysts, where TOF was turnover frequency. As shown in Fig. 3b, the TOF_{Fe} of $\text{Fe}_2\text{P-NPs/NC}$ ($346.4\text{ L min}^{-1}\text{ g}^{-1}$) and Fe-SAs/PNC ($518.2\text{ L min}^{-1}\text{ g}^{-1}$) are higher than Fe-NPs/NC ($49.8\text{ L min}^{-1}\text{ g}^{-1}$)

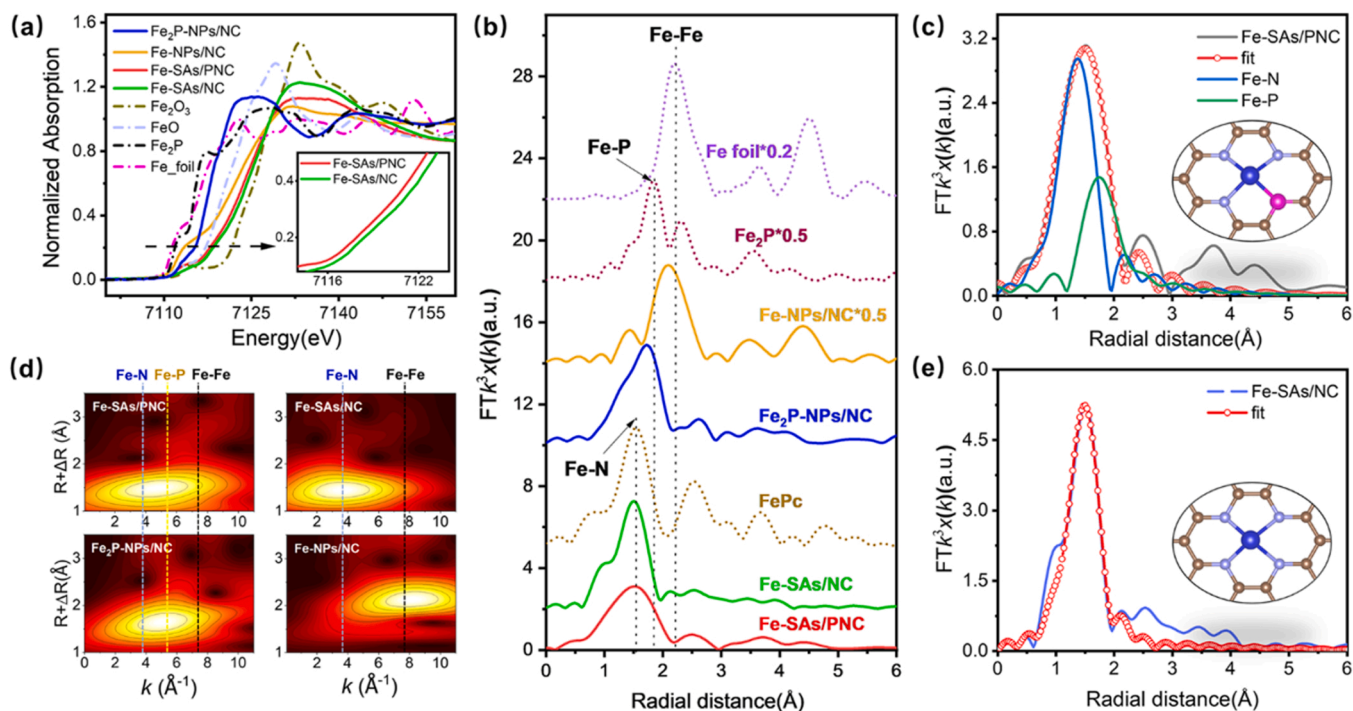


Fig. 2. (a) Normalized Fe K-edge XANES spectra of $\text{Fe}_2\text{P-NPs/NC}$, Fe-SAs/PNC, Fe-NPs/NC, Fe-SAs/NC, and the reference samples (Fe foil, FeO, and Fe_2O_3). (b) Fe K-edge FT-EXAFS spectra of $\text{Fe}_2\text{P-NPs/NC}$, Fe-SAs/PNC, Fe-NPs/NC, Fe-SAs/NC, and reference samples (Fe foil, FePc, and Fe_2P). (c) k^3 -weight FT-EXAFS fitting curves of Fe-SAs/PNC. (d) WT-EXAFS plots of $\text{Fe}_2\text{P-NPs/NC}$, Fe-SAs/PNC, Fe-NPs/NC, and Fe-SAs/NC. (e) k^3 -weight FT-EXAFS fitting curves of Fe-SAs/NC.

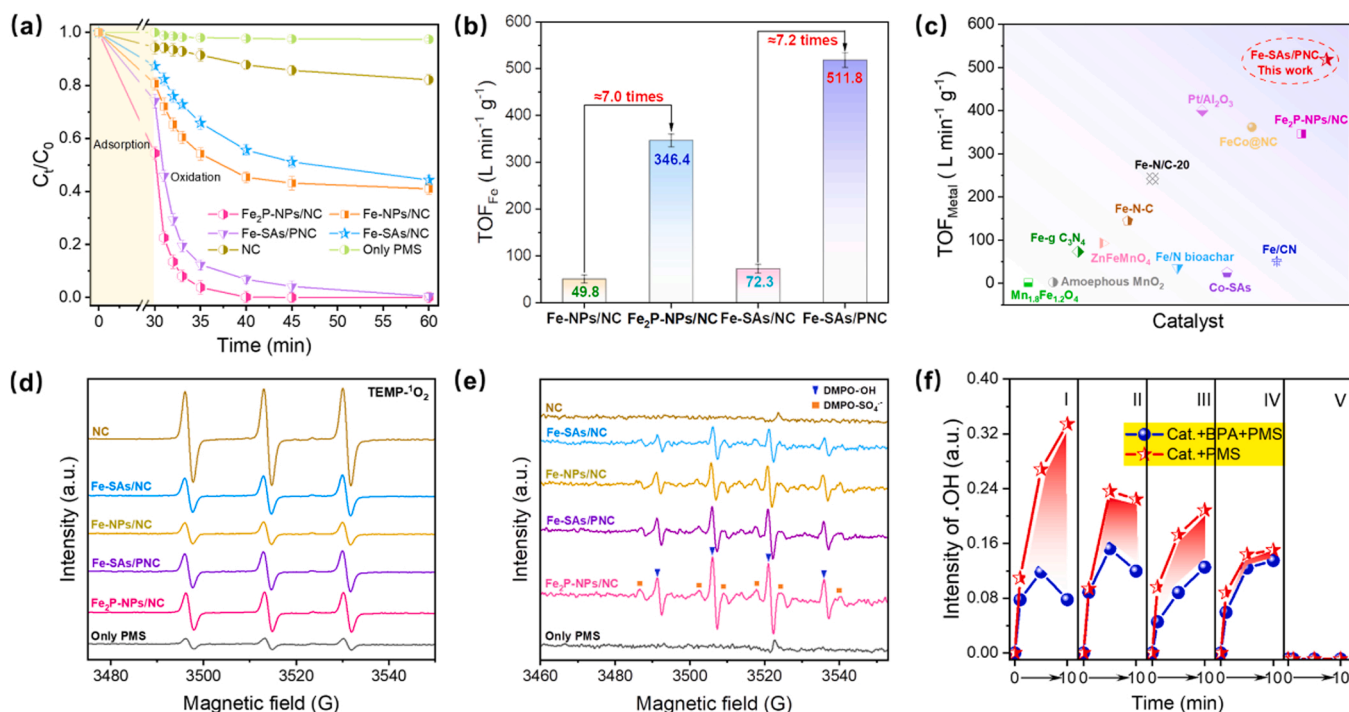


Fig. 3. (a) Performances of different catalysts for the degradation of BPA ([BPA] = 10 mg L⁻¹, [PMS] = 0.15 g L⁻¹, [catalyst] = 0.1 g L⁻¹). (b) Comparison of the TOF_{Fe} of Fe₂P-NPs/NC, Fe-SAs/PNC, Fe-NPs/NC, and Fe-SAs/NC. (c) Comparison of the TOF_{Fe} of Fe₂P-NPs/NC and Fe-SAs/PNC with reported catalysts from the literature. (d) ESR spectrum of TEMP-¹O₂ radical. (e) ESR spectrum of DMPO-•OH and DMPO-SO₄^{•-} adducts. (f) ESR spectra of DMPO-•OH signal intensities in the catalyst+PMS and catalyst+BPA+PMS systems at different catalytic times (I: Fe₂P-NPs/NC, II: Fe-SAs/PNC, III: Fe-NPs/NC, IV: Fe-SAs/NC, V: NC).

g⁻¹) and Fe-SAs/NC (72.3 L min⁻¹ g⁻¹), indicating that P-doping significantly improved the catalytic activity of Fe NPs and SAs catalysts. As shown in Fig. 3c and Table S3, the TOF_{Fe} of Fe-SAs/PNC are markedly higher than those of similar reported Fe-based heterogeneous catalysts. In addition, the content of Fe dissolved in the solution after reaction was extremely low (< 30 µg L⁻¹) (Fig. S11) so that the same concentration of Fe²⁺ in homogeneous system was nearly unable to degrade BPA effectively. The controlling experiments presented the same result that the addition of Fe²⁺ with the same concentration could not improve the catalytic efficiency of NC+PMS system (Fig. S12a). These results indicate that the effective catalytic reactions occurred at the site of Fe NPs and SAs in the catalysts. Furthermore, a positive correlation was observed between the adsorption efficiency of BPA and k_{obs} (Fig. S13), indicating that the excellent pollutant oxidation performance should be attributed to the synergistic effect of adsorption and oxidation processes. Therefore, when PMS and BPA were added simultaneously, the degradation efficiency of BPA was significantly reduced (Fig. S12b). As shown in Fig. S14, all the tested anions (Cl⁻, HCO₃⁻, H₂PO₄⁻, NO₃⁻) and HA (< 20 mg L⁻¹) did not obviously influence the degradation of BPA, which should be caused by the strong adsorption of BPA on the catalyst that promoted the degradation of BPA by ROS in a shorter distance (take Fe-SAs/PNC as example). To investigate the performance of Fe-SAs/PNC on degradation of other organic pollutants, different types of concerned organics, including benzoic acid (BA), sulfamethoxazole (SMX), nitrobenzene (NP), ibuprofen (IBP), and Carbamazepine (CBZ), were also tested. As shown in Fig. S15 all pollutants were effectively degraded. Furthermore, the Fe-SAs/PNC exhibits a slight decrease toward the degradation of BPA after five cycles (Fig. S16), suggesting that the stability of catalyst could effectively support the cyclic utilization in practical application.

3.3. Identification of active species

To identify the reactive oxygen species (ROS) generated during PMS

activation, electron spin resonance spectroscopy (ESR) was used for catalyst+PMS systems. As shown in Fig. 3d, the TEMP-¹O₂ signals of four catalysts were obviously lower than that of NC, indicating that the singlet oxygen might be generated by the nitrogen-carbon skeleton. [38] By contrast, the strong DMPO-•OH signals and weak DMPO-SO₄^{•-} signals were observed for all catalysts, while neither of the two ROS were detected for NC (Fig. 3e). In addition, the introduction of P markedly enhanced the activation capacities of Fe-NPs and Fe-SAs on PMS for generating hydroxyl radicals and sulfate radicals. Furthermore, no superoxide was detected for each catalyst in methanol solution by using DMPO as trapping reagent (Fig. S18). To detect the effective ROS types for BPA degradation, quenching experiments were performed for catalyst+BPA+PMS systems. As shown in Fig. S19, the addition of excess methanol (MeOH, scavenger for •OH and SO₄^{•-}) or tert-butanol (TBA, •OH scavenger) extremely inhibited the degradation of BPA, while only weak and neglect inhibition effects were induced by L-histidine (¹O₂ scavenger) and benzoquinone (BQ, superoxide radical scavenger) for Fe-SAs/PNC. The same results were obtained for all other catalysts. To check the contribution of high-valent iron in the reaction, PMSO was used as a chemical probe to detect the existence of high-valent iron. As shown in Fig. S20, the yield of PMSO₂ were only increased about ~3 % for the all catalyst+PMS systems compared to the bare PMS system, indicating that the high-valent iron was not produced in those systems [39,40]. These results absolutely confirm that •OH was the dominant ROS in degrading BPA for all catalysts. Furthermore, the changes of •OH content with reaction time in different reaction systems were calculated based on ESR signal intensities (Fig. 3f and Fig. S21). In the absence of BPA, the highest signal intensity was obtained for Fe₂P-NPs/NC, followed by Fe-SAs/PNC, Fe-NPs/NC, and Fe-SAs/NC. When BPA was added, the signal intensities of •OH were apparently weakened due to the consumption of •OH for degrading BPA. The results are in good consistence with the BPA degradation experiments.

The adsorption of PMS on the catalyst surface is the key and primary condition for its activation. Therefore, the in-situ Raman technique was applied to characterize the adsorption process of PMS on the catalysts.

As shown in Fig. 4a, there are three characteristic peaks at 881 cm^{-1} , 979 cm^{-1} and 1059 cm^{-1} for PMS solution, corresponding to the stretching vibration of the O-O bond in (HSO_5^-) , the symmetric stretching vibration of SO_4^{2-} and the symmetric stretching vibration of SO_3 (HSO_3^-), respectively. Compared to the NC/PMS system, the three characteristic peaks were enhanced for all Fe-based catalyst+PMS systems, indicating that Fe-based catalysts behaved stronger adsorption capacities than NC. Accordingly, the peaks for O-O bond shifted from 881 cm^{-1} to 890 cm^{-1} and SO_3 peaks shifted from 1059 cm^{-1} to 1052 cm^{-1} after PMS was absorbed by the catalysts due to the interaction between PMS and catalysts. As the intensity of SO_4^{2-} peaks increased more obviously than another two peaks, it can be concluded that the PMS partially decomposed after absorbed on the Fe-based catalysts. This conclusion is further supported by the PMS consumption experiments. As shown in Fig. 4b, for the NC+PMS system, the consumption of PMS increased slowly with increasing initial PMS concentration, while the consumption of PMS in $\text{Fe}_2\text{P-NPs/NC}$ +PMS system increased significantly with the increase of initial PMS concentration. The same results obtained for other catalysts (Fig. S22), which are corresponding with the increase of k_{obs} as shown in Fig. S23. Furthermore, the P-doped catalysts behaved stronger adsorption and catalysis capacities for PMS than control catalyst groups, which was consistent with BPA degradation experiments.

Chronoamperometry analysis was used to further explore the charge transfer processes among catalysts and reactants. As shown in Fig. 4c, when PMS was injected into the Fe-based catalyst solutions, the current dropped rapidly (this current jump was denoted as $\Delta I_{\text{Cat-PMS}^*}$), indicating that the electrons flowed from the catalysts to PMS after PMS was rapidly captured by the catalysts. After that, the current gradually rose and reached plateaus in tens of seconds, due to the decomposition of the

intermediates Cat-PMS^* accompanied with the fall-off of resultants from the surface of catalysts. Subsequently, the current rapidly jumped from negative to positive (this current jump was denoted as $\Delta I_{\text{Cat-BPA}}$) after BPA was added, where the electrons transferred from BPA to the catalysts and PMS began to decompose rapidly. The electron transfer routes are further proved by the changes of zeta potential for the catalysts (Fig. S24). The $\Delta I_{\text{Cat-PMS}^*}$ of Fe-based catalysts are obviously higher than that of NC, which further demonstrates that the Fe-based catalyst perform the stronger interaction with PMS and higher electron transfer ability. Moreover, the $\Delta I_{\text{Cat-PMS}^*}$ of $\text{Fe}_2\text{P-NPs/NC}$ and Fe-SAs/PNC are $6.8\text{ }\mu\text{A}$ and $2.4\text{ }\mu\text{A}$, which are significantly higher than those of the control catalysts without P-doping (1.15 and $0.64\text{ }\mu\text{A}$). The good electron transfer capability is attributed to the excellent electrical conductivity, which can be inferred from the results of the electrochemical impedance spectrum (EIS) (Fig. S25). It can be seen that the arc diameters of $\text{Fe}_2\text{P-NPs/NC}$ and Fe-SAs/PNC are much smaller than those of Fe-NPs/NC and Fe-SAs/NC , indicating that the P-doping effectively lowered the electron transfer resistance by improving the acceptance/donation ability of Fe active sites. This conclusion can be further confirmed by the results of linear voltammetry curve (CV) test (Fig. S26). In addition, as shown in Fig. 4f, the normalized PMS consumption ($\text{PMS}_{\text{cons}}/\text{m}_{\text{catalyst}}$) and the cumulative intensity of $\bullet\text{OH}$ signal ($\Delta I_{\text{DMPO-}\bullet\text{OH}}$) are strongly and positively related to $\Delta I_{\text{Cat-PMS}^*}$. Therefore, it can be deduced that the P-doping enhanced the PMS adsorption and electron transfer capabilities of Fe NPs and SAs catalysts so that $\bullet\text{OH}$ could be rapidly and massively generated due to effective electron transfer mechanism.

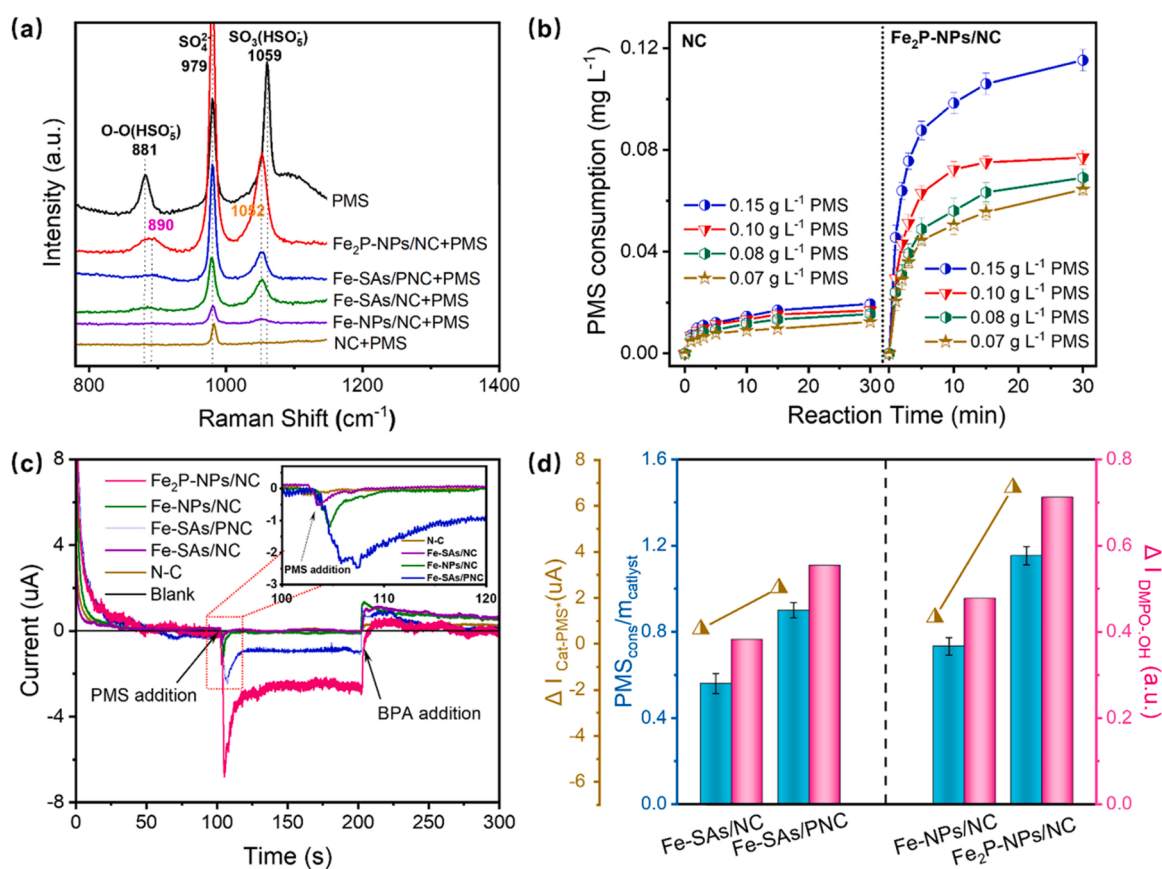


Fig. 4. (a) In situ Raman spectrum in the catalyst+PMS systems. (b) PMS consumption in NC+PMS and $\text{Fe}_2\text{P-NPs/NC}$ +PMS systems with different initial PMS doses. (c) Amperometric i-t curve measurements upon the addition of PMS and BPA with the different catalysts. (d) Relationship between $\Delta I_{\text{DMPO-}\bullet\text{OH}}$ with $\text{PMS}_{\text{cons}}/\text{m}_{\text{catalyst}}$ and $\Delta I_{\text{Cat-PMS}^*}$ in different PMS activation systems. (The consumption of PMS includes both parts of adsorption and decomposition by catalyst.).

3.4. Role of BPA adsorption on its degradation

Based on the above discussion, the adsorption of BPA played an important role in catalytic and degradation processes. Herein, Fe-SAs/PNC was selected as the research target. As shown in Fig. 5a, the broad peaks at 1571.3 cm^{-1} and 1209.0 cm^{-1} corresponding to the C=C group and C-N/C-H group are present in the FT-IR spectrum.[41, 42] After interacting with BPA, both of the peaks shifted to the new wavenumbers (1571.1 cm^{-1} and 1209.0 cm^{-1}), and two new peaks appeared at 1511.1 cm^{-1} and 830.1 cm^{-1} , which could be attributed to the BPA.[43] After PMS was added, the peak at 1511.1 cm^{-1} and 830.1 cm^{-1} disappeared and the C=C and C-N/C-H peaks returned to their initial position, indicating that the BPA on the catalyst surface was effectively decomposed. However, this phenomenon did not occur obviously in NC system, due to the weak interaction between NC and BPA (Fig. S27). Furthermore, the contents of pyridinic N, pyrrolic N, graphitic N, Fe-N and oxidized N were characterized by XPS technique for the catalysts. As shown in Fig. S28, the peak at 398.3 eV, 399.0 eV, 400.1 eV, 401.1 eV, and 403.0 eV are corresponding to pyridinic N, Fe-N, pyrrolic N, graphitic N and oxidized N, respectively.[44–46] As shown in Fig. 5b, the adsorption quantity of BPA and the content of graphitic N display the closest correlation, indicating that graphitic N might act as the adsorption site for BPA. To confirm this conclusion, a further investigation was carried out during cyclic utilization test. As shown in Fig. 5c, the BPA adsorption amount decreased from 25.8 % to 17.5 %, while the graphitic N content of Fe-SAs/PNC decreased from 37.15 % to 32.21 % after the catalyst was directly used for the second time (Fig. 5d). However, after simple annealing treatment, the graphitic N content of Fe-SAs/PNC could recover from 32.21 % to 36.74 %, and the BPA adsorption amount was also elevated from 17.5 % to 22.9 %, further verifying that the graphitic N should be the adsorption site for BPA. As discussed above, the addition of BPA led to the change of current in chronoamperometry test, where electrons transferred from BPA

to the catalysts. As shown in Fig. 5e, the $\Delta I_{\text{Cat-BPA}}$ of the NC is significantly lower than those of other Fe-based catalysts, indicating that the Fe element improved the electron transfer process and might be the terminal electron acceptor. Besides that, the introduction of P element effectively enhanced this process. Combined with the results of quenching experiments, it can be inferred that BPA (electron donor) could transfer electrons to the catalysts, which accelerated the electron cyclic process in PMS activation and BPA degradation reactions. This is an auxiliary pathway to degrade BPA besides the dominant $\bullet\text{OH}$ oxidation process (Fig. 5f).

3.5. Theoretical calculations and analysis

In order to clarify the effect of P-doping on the catalytic activity of Fe-based catalysts in depth, the DFT calculation was performed to reveal the intrinsic relationship between electron structure of Fe and PMS activation capacity. Firstly, the adsorption energy (E_{ads}) levels were evaluated for four target catalysts. As shown in Fig. 6a, the $|E_{\text{ads}}|$ for the adsorption of PMS on Fe-P₁N₃ site (1.3536 eV) is much higher than Fe-N₄ site (0.6613 eV), indicating that the PMS molecule was more easily and stably adsorbed on Fe SA site after P was introduced.[47] The same result was obtained for the catalysts containing Fe and Fe₂P NPs (Table S4). Secondly, the charge transfer amount (Q_e) from Fe active site to PMS was calculated from electron density difference data, the result of which shown that the Q_e were all elevated for Fe SA and NPs after P was doped surrounding Fe atoms (Table S4). More charge transfer means that the PMS molecule is easier to acquire electron in activation reaction and generates ROS subsequently. In addition, the O-O bond in PMS was elongated after PMS was adsorbed on Fe site, where P-doping led to a larger elongation of O-O bond for both SA and NPs catalysts (Table S4 and Fig. S29). Therefore, the DFT calculation results clearly show that the P-doping can effectively improve the catalytic capability of Fe-based catalysts by enhancing the adsorption and charge transfer

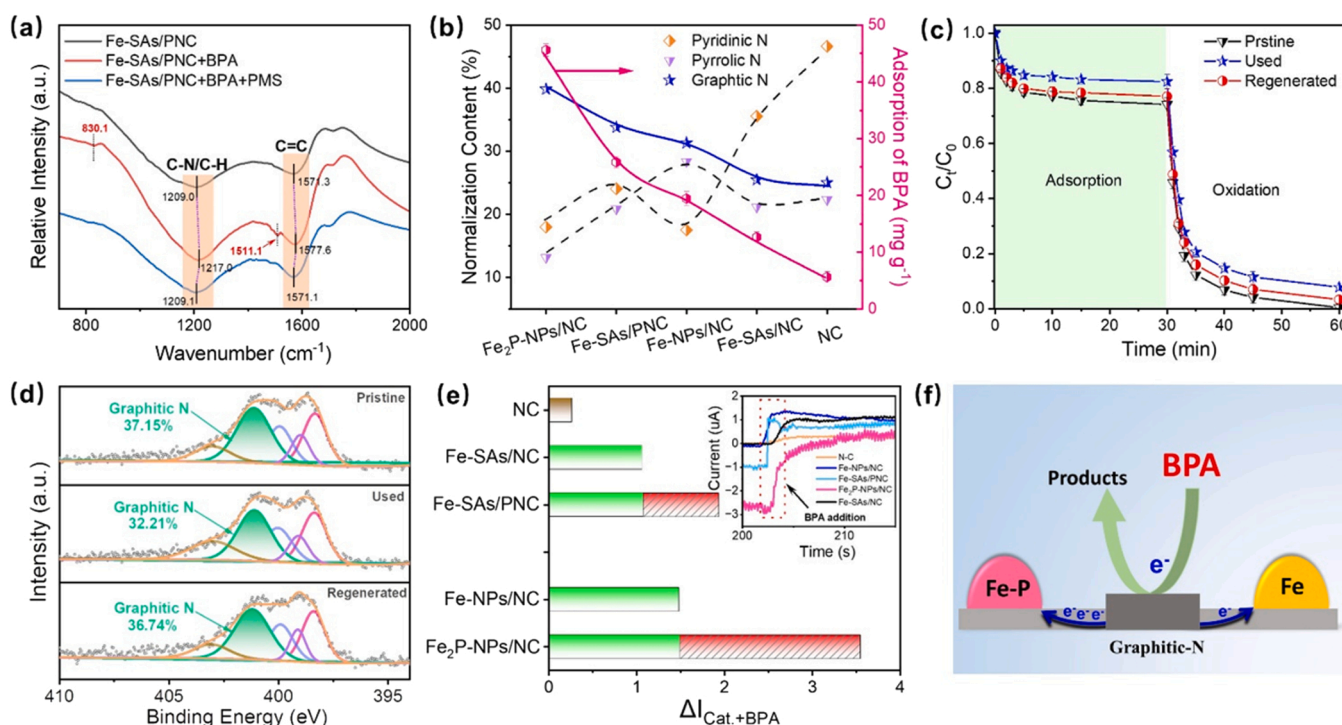


Fig. 5. (a) FT-IR spectra of Fe-SAs/PNC and NC after reaction with BPA and PMS. (b) Relationship between the BPA adsorption capacity and the N contents for Fe₂P-NPs/NC, Fe-SAs/PNC, Fe-NPs/NC and Fe-SAs/NC. (c) The performance of pristine/used/regenerated Fe-SAs/PNC for BPA adsorption and oxidation (The catalyst was annealed at 600 °C in Ar atmosphere to recovery catalytic activity). (d) High-resolution N 1s XPS spectra of pristine/used/regenerated Fe-SAs/PNC. (e) The $\Delta I_{\text{Cat-BPA}}$ in different catalyst+BPA+PMS systems. (f) Schematic illustration of the BPA adsorption and its decomposition (left: the P doped Fe-based catalysts; right: the P undoped Fe-based catalysts).

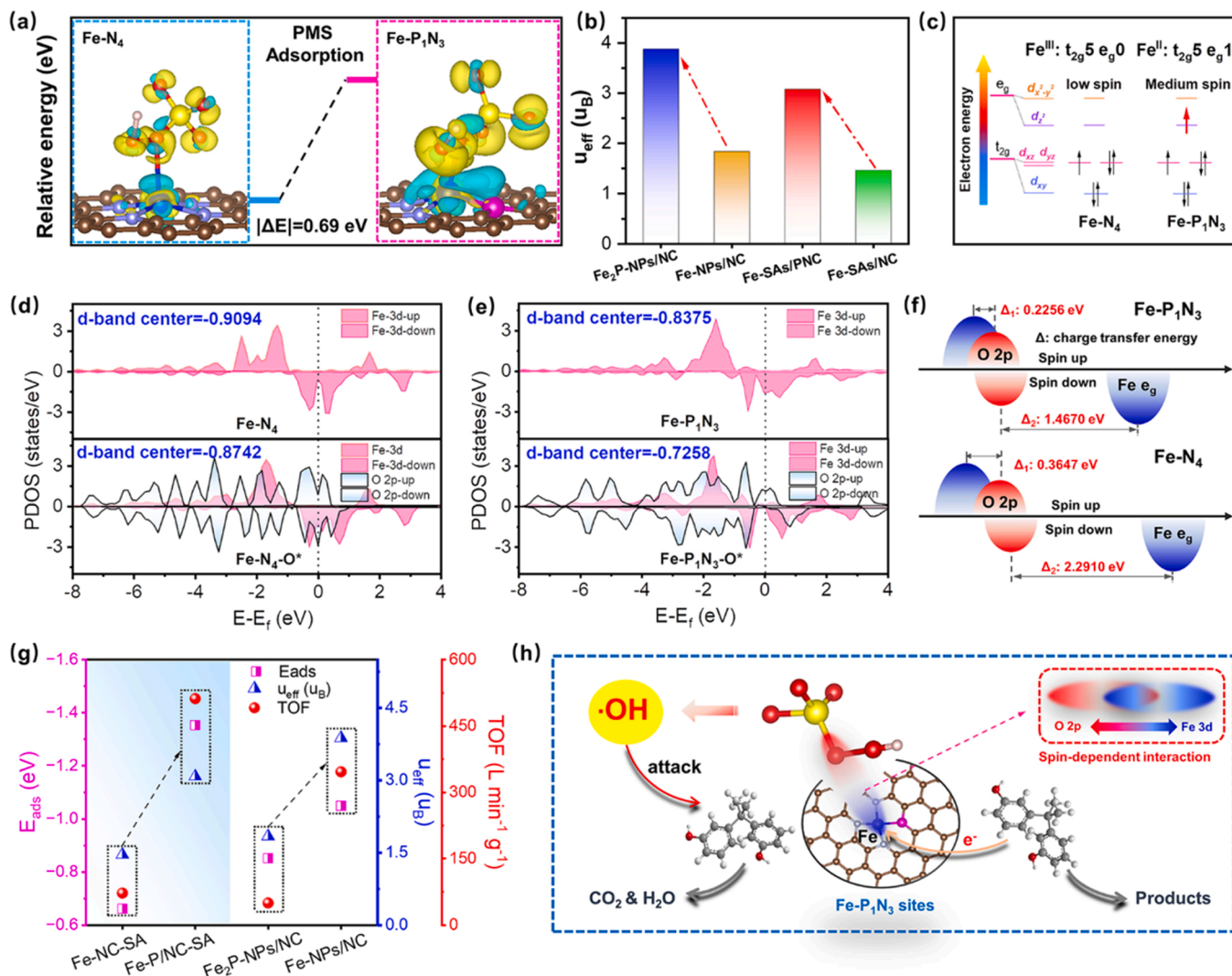


Fig. 6. (a) The calculated electron density difference diagrams of Fe-SAs/PNC and Fe-SAs/NC with PMS adsorbed on the Fe site (Yellow and blue represent electron gain and loss, respectively). (b) The μ_{eff} of Fe₂P-NPs/NC, Fe-SAs/PNC, Fe-NPs/NC, and Fe-SAs/NC. (c) Schematic representation of the spin transition of part of Fe-P₁N₃ and Fe-N₄. The projected electronic density of states for (d) Fe-SAs/PNC and (e) Fe-SAs/NC. (f) Schematic representation of the Fe 3d and O 2p-band centers for (up) Fe-P₁N₃ and (down) Fe-N₄. (g) Correlation between E_{ads} , μ_{eff} and TOF_{Fe} of the catalysts. (h) Schematic illustration of the catalytic activation mechanism of Fe-SAs/PNC.

capabilities of Fe active sites.

Actually, the catalytic activity is the external performance relating to the internal nature of Fe active site. The electron structures of the catalysts were then investigated to get an insight into the effect of P-doping. As shown in Fig. S30, it can be seen that the doped P effectively increase the electron density of the Fe atoms both in SA and NPs catalysts, which is in consistence with the valence analysis results of XANES spectra (Fig. S8). The XPS results (Fig. S31) also confirm this fact that Fe-SAs/PNC contains more Fe^{II} than Fe-SAs/NC (Fe^{II}/Fe^{III} ratio of 2.82 vs 1.13). In addition, the DFT results (Fig. 6d and e) show that the projected density of states (PDOS) of Fe-P₁N₃ shift toward the positive direction with a higher d-band center (-0.8375 eV) compared to Fe-N₄ (-0.9094 eV), indicating that the existence of P increases the Fe 3d band energy. Furthermore, the PDOS of Fe in Fe-P₁N₃ moves to the higher energy direction and d-band center is elevated to -0.7258 eV after adsorption of PMS. As the overlap between the Fe 3d orbital of Fe-P₁N₃ and the O 2p orbital of PMS is larger than that of Fe-N₄ (Fig. 6f), it is expected that the electrons can transfer from Fe centers to PMS molecules more easily and smoothly. The similar phenomenon was observed for the PDOS of the Fe₂P and Fe NPs models (Fig. S32 and Table S5).

The shift of Fe PDOS to the higher energy direction is usually

accompanied by the variation of spin state for Fe 3d electrons. To get a direct experiment proof, the effective magnetic moments (μ_{eff}) of the four catalysts were calculated from $\chi^{-1}-T$ curves (Fig. S33 and S34). As shown in Fig. 6b, the μ_{eff} of Fe SA and NPs were significantly increased by doping P around Fe active centers. According to the theoretical calculation equation for μ_{eff} , the spin number and unpaired electron number for the target catalysts were estimated from experimental data (Table S6). As the Fe-N₄ and Fe-P₁N₃ single atom models could be practically analyzed by coordination field theory, it can be deduced that the Fe species in Fe-SAs/NC are loaded with LS state ($t_{2g}^5e_g^0$), while the Fe species in Fe-SAs/PNC hold a medium spin state (Fig. 6c). That is to say, the P-doping not only increased the electron density of Fe SAs, but also increased the amount of the unpaired electrons. For Fe₂P-NPs/NC and Fe-NPs/NC, the electron density of states results clearly shown that Fe element in Fe₂P has fewer 3d electrons between the up and down states (Fig. S35), demonstrating that the P-doping also effectively increase the unpaired electrons in Fe NPs and induce the change of spin state for Fe 3d electrons. This result is indeed consistent with experimental μ_{eff} values and relative parameters (Table S6). Furthermore, the electron density at Fe center in Fe₂P NPs is more dispersed than Fe NPs (Fig. S30), indicating that the introduction of P element induced the

localized delocalization of Fe 3d electrons, suggesting that the P-doping can potentially advance the transfer of 3d electrons from Fe to the O 2p orbital.

As shown in Fig. 6g, the TOF_{Fe} and E_{ads} both increased with the increase of μ_{eff} for SAs and NPs catalysts. For PMS activation, the P-doping increased the energy of Fe 3d electrons, which allowed the electrons to transfer from Fe to O 2p orbital of PMS more easily. Since the rise of electron energy should be led by the unpaired electrons in the high energy orbitals, it can be deduced that μ_{eff} can be regarded as an important indicator for evaluating the catalytic capability of one Fe-based catalyst. In another words, the increase of the unpaired electrons induced by P-doping (corresponding to the phenomenon that the spin state transforms from LS to MS) is the key factor to enhance the activation of PMS. Therefore, as shown in Fig. 6h, the mechanism for the enhancement of PMS activation and BPA degradation led by P-doping was proposed based on the experimental results and theoretical calculations by taking Fe-SAs/PNC as an example. By introducing P element toward Fe active sites, the spin state of Fe is converted to a MS state accompanied by the generation of more unpaired electrons with high energy, which permits the Fe 3d orbital to better overlap with the O 2p orbital of PMS after the PMS molecules are absorbed on Fe sites. Then the unpaired electrons in e_g orbitals come into the O 2p orbitals of PMS, leading to breakage of the O-O bond in PMS and the formation of $\bullet\text{OH}$ by one-electron transfer. In addition, the P-doping also increase the amount of graphitic N that is beneficial for the adsorption of BPA, promoting the electron transfer process from BPA (electron donor) to the Fe active sites. Based on the quenching experiments, it can be seen that BPA was degraded mainly via $\bullet\text{OH}$ oxidation pathway, and the electron transfer reaction from BPA to Fe advanced this process.

4. Conclusions

In summary, this study found that the P-doping could significantly improve the capability of Fe-based heterogeneous catalysts for enhancing the activation of PMS and degradation of BPA. To clearly explore the intrinsic mechanism of this phenomenon, the comparative group catalysts involving Fe-based SA catalysts and NPs catalysts, were successfully prepared by using an in-situ phosphorylation strategy based on the confinement effect. Experimental investigations and DFT calculations reveal that P-doping operation can effectively modulate the electronic structure of Fe active sites, which further markedly enhance the catalytic performance for PMS activation. The introduction of P element toward Fe increased the energy of the Fe 3d orbital electrons and promoted the generation of more unpaired electrons accompanied by transformation of spin state from LS to MS state. This allowed the Fe 3d orbitals to better overlap with the O 2p orbitals of PMS, successfully realizing the activation of PMS by electron transfer from Fe to PMS. Then the O-O bond of PMS was broken and $\bullet\text{OH}$ was generated subsequently to further degrade BPA. Furthermore, the P-doping also increased the amount of graphitic N in the carbon support for absorbing more BPA, which facilitated the electron transfer process from BPA to Fe and charge recycling of Fe active sites. As the P-doping strategy was available for both Fe SA and NPs catalysts, this study provides a general understanding of the principle for electronic structure modulation by doping P to Fe active centers and the structure-activity relationship for PMS-AOPs at the atomic level, which is beneficial to instruct the development of Fe-based catalysts with high function.

CRediT authorship contribution statement

Zhaoyi Yang: Conceptualization, Methodology, Formal analysis, Investigation, Writing - original draft, Visualization. **Xiaofang Yang:** Writing - review & editing, Supervision. **Guanyu An:** Writing - review & editing, Supervision. **Dongsheng Wang:** Resources, Supervision.

Declaration of Competing Interest

The authors declare that they have no known competing financial interests or personal relationships that could have appeared to influence the work reported in this paper.

Data availability

Data will be made available on request.

Acknowledgments

The work was supported by the National Natural Science Foundation of China (52030003). We thank Prof. Guangzhi He from Research Center for Eco-Environmental Sciences, Chinese Academy of Sciences, Prof. Wu shuqi from Kyushu University and Prof. Xi jinyang from Shanghai University for the suggestions in the DFT calculation. The XAFS measurements made use of the resources of National Synchrotron Radiation Laboratory in Beijing.

Appendix A. Supporting information

Supplementary data associated with this article can be found in the online version at doi:10.1016/j.apcatb.2023.122618.

References

- [1] V.I. Parvulescu, F. Epron, H. Garcia, P. Granger, Recent progress and prospects in catalytic water treatment, *Chem. Rev.* 122 (2022) 2981–3121.
- [2] Y. Shang, X. Xu, B. Gao, S. Wang, X. Duan, Single-atom catalysis in advanced oxidation processes for environmental remediation, *Chem. Soc. Rev.* 50 (2021) 5281–5322.
- [3] Q. Wu, H. Yang, L. Kang, Z. Gao, F. Ren, Fe-based metal-organic frameworks as Fenton-like catalysts for highly efficient degradation of tetracycline hydrochloride over a wide pH range: acceleration of Fe(II)/Fe(III) cycle under visible light irradiation, *Appl. Catal. B: Environ.* 263 (2020).
- [4] I.A. Ike, K.G. Linden, J.D. Orbell, M. Duke, Critical review of the science and sustainability of persulphate advanced oxidation processes, *Chem. Eng. J.* 338 (2018) 651–669.
- [5] H. Li, C. Shan, B. Pan, Fe(III)-doped g-C₃N₄ mediated peroxymonosulfate activation for selective degradation of phenolic compounds via high-valent iron-oxo species, *Environ. Sci. Technol.* 52 (2018) 2197–2205.
- [6] C. Zhao, L. Meng, H. Chu, J.-F. Wang, T. Wang, Y. Ma, C.-C. Wang, Ultrafast degradation of emerging organic pollutants via activation of peroxymonosulfate over Fe₃C/Fe@N-C-x: Singlet oxygen evolution and electron-transfer mechanisms, *Appl. Catal. B-Environ.* 321 (2023).
- [7] X.-W. Zhang, M.-Y. Lan, F. Wang, C.-C. Wang, P. Wang, C. Ge, W. Liu, Immobilized N-C/Co derived from ZIF-67 as PS-AOP catalyst for effective tetracycline matrix elimination: from batch to continuous process, *Chem. Eng. J.* 450 (2022).
- [8] F. Wang, H. Fu, F.X. Wang, X.W. Zhang, P. Wang, C. Zhao, C.C. Wang, Enhanced catalytic sulfamethoxazole degradation via peroxymonosulfate activation over amorphous CoS_x@SiO₂ nanocages derived from ZIF-67, *J. Hazard Mater.* 423 (2022), 126998.
- [9] Y. Gao, C. Yang, M. Zhou, C. He, S. Cao, Y. Long, S. Li, Y. Lin, P. Zhu, C. Cheng, Transition metal and metal-N_x codoped MOF-derived fenton-like catalysts: a comparative study on single atoms and nanoparticles, *Small* 16 (2020), e2005060.
- [10] X. Mi, P. Wang, S. Xu, L. Su, H. Zhong, H. Wang, Y. Li, S. Zhan, Almost 100% peroxymonosulfate conversion to singlet oxygen on single-atom CoN_{2-x} sites, *Angew. Chem. Int. Ed. Engl.* 60 (2021) 4588–4593.
- [11] J. Lee, U. von Gunten, J.H. Kim, Persulfate-based advanced oxidation: critical assessment of opportunities and roadblocks, *Environ. Sci. Technol.* 54 (2020) 3064–3081.
- [12] H. Zhou, H. Zhang, Y. He, B. Huang, C. Zhou, G. Yao, B. Lai, Critical review of reductant-enhanced peroxide activation processes: trade-off between accelerated Fe³⁺/Fe²⁺ cycle and quenching reactions, *Appl. Catal. B: Environ.* 286 (2021).
- [13] M. Zhang, C. Xiao, X. Yan, S. Chen, C. Wang, R. Luo, J. Qi, X. Sun, L. Wang, J. Li, Efficient removal of organic pollutants by metal-organic framework derived Co/C yolk-shell nanoreactors: size-exclusion and confinement effect, *Environ. Sci. Technol.* 54 (2020) 10289–10300.
- [14] J. Wang, B. Li, Y. Li, X. Fan, F. Zhang, G. Zhang, W. Peng, Facile synthesis of atomic Fe-N-C materials and dual roles investigation of Fe-N₄ sites in fenton-like reactions, *Adv. Sci.* 8 (2021), e2101824.
- [15] Z. Tang, P. Zhao, H. Wang, Y. Liu, W. Bu, Biomedicine meets fenton chemistry, *Chem. Rev.* 121 (2021) 1981–2019.
- [16] L. Liu, A. Corma, Metal catalysts for heterogeneous catalysis: from single atoms to nanoclusters and nanoparticles, *Chem. Rev.* 118 (2018) 4981–5079.

- [17] Z. Li, S. Ji, Y. Liu, X. Cao, S. Tian, Y. Chen, Z. Niu, Y. Li, Well-defined materials for heterogeneous catalysis: from nanoparticles to isolated single-atom sites, *Chem. Rev.* 120 (2020) 623–682.
- [18] S.K. Kaiser, Z. Chen, D. Faust Akl, S. Mitchell, J. Perez-Ramirez, Single-atom catalysts across the periodic table, *Chem. Rev.* 120 (2020) 11703–11809.
- [19] Z.W. Seh, J. Kibsgaard, C.F. Dickens, I. Chorkendorff, J.K. Nørskov, T.F. Jaramillo, Combining theory and experiment in electrocatalysis: insights into materials design, *Science* 355 (2017).
- [20] Y. Zhu, J. Sokolowski, X. Song, Y. He, Y. Mei, G. Wu, Engineering local coordination environments of atomically dispersed and heteroatom-coordinated single metal site electrocatalysts for clean energy-conversion, *Adv. Energy Mater.* 10 (2019).
- [21] G. Shen, R. Zhang, L. Pan, F. Hou, Y. Zhao, Z. Shen, W. Mi, C. Shi, Q. Wang, X. Zhang, J.J. Zou, Regulating the spin state of Fe(III) by atomically anchoring on ultrathin titanium dioxide for efficient oxygen evolution electrocatalysis, *Angew. Chem. Int. Ed. Engl.* 59 (2020) 2313–2317.
- [22] Y. Han, Y. Wang, R. Xu, W. Chen, L. Zheng, A. Han, Y. Zhu, J. Zhang, H. Zhang, J. Luo, C. Chen, Q. Peng, D. Wang, Y. Li, Electronic structure engineering to boost oxygen reduction activity by controlling the coordination of the central metal, *Energy Environ. Sci.* 11 (2018) 2348–2352.
- [23] W. Zhong, Y. Qiu, H. Shen, X. Wang, J. Yuan, C. Jia, S. Bi, J. Jiang, Electronic spin moment as a catalytic descriptor for Fe single-atom catalysts supported on C₂N, *J. Am. Chem. Soc.* 143 (2021) 4405–4413.
- [24] Z.-y. Mei, S. Cai, G. Zhao, Q. Jing, X. Sheng, J. Jiang, H. Guo, Understanding electronic configurations and coordination environment for enhanced ORR process and improved Zn-air battery performance, *Energy Storage Mater.* 50 (2022) 12–20.
- [25] X. Li, C.-S. Cao, S.-F. Hung, Y.-R. Lu, W. Cai, A.I. Rykov, S. Miao, S. Xi, H. Yang, Z. Hu, J. Wang, J. Zhao, E.E. Alp, W. Xu, T.-S. Chan, H. Chen, Q. Xiong, H. Xiao, Y. Huang, J. Li, T. Zhang, B. Liu, Identification of the electronic and structural dynamics of catalytic centers in single-Fe-atom material, *Chem* 6 (2020) 3440–3454.
- [26] S. Sun, G. Shen, J. Jiang, W. Mi, X. Liu, L. Pan, X. Zhang, J.J. Zou, Boosting oxygen evolution kinetics by Mn-N-C motifs with tunable spin state for highly efficient solar-driven water splitting, *Adv. Energy Mater.* 9 (2019).
- [27] Y. Sun, S. Sun, H. Yang, S. Xi, J. Gracia, Z.J. Xu, Spin-related electron transfer and orbital interactions in oxygen electrocatalysis, *Adv. Mater.* 32 (2020), e2003297.
- [28] Z.Y. Guo, Y. Si, W.Q. Xia, F. Wang, H.Q. Liu, C. Yang, W.J. Zhang, W.W. Li, Electron delocalization triggers nonradical Fenton-like catalysis over spinel oxides, *Proc. Natl. Acad. Sci. USA* 119 (2022), e2201607119.
- [29] X. Zhou, M.K. Ke, G.X. Huang, C. Chen, W. Chen, K. Liang, Y. Qu, J. Yang, Y. Wang, F. Li, H.Q. Yu, Y. Wu, Identification of Fenton-like active Cu sites by heteroatom modulation of electronic density, *Proc. Natl. Acad. Sci. USA* 119 (2022).
- [30] L. Jiao, W. Xu, Y. Zhang, Y. Wu, W. Gu, X. Ge, B. Chen, C. Zhu, S. Guo, Boron-doped Fe-N-C single-atom nanozymes specifically boost peroxidase-like activity, *Nano Today* 35 (2020).
- [31] P. Shao, S. Yu, X. Duan, L. Yang, H. Shi, L. Ding, J. Tian, L. Yang, X. Luo, S. Wang, Potential difference driving electron transfer via defective carbon nanotubes toward selective oxidation of organic micropollutants, *Environ. Sci. Technol.* 54 (2020) 8464–8472.
- [32] W. Ren, L. Xiong, G. Nie, H. Zhang, X. Duan, S. Wang, Insights into the electron-transfer regime of peroxydisulfate activation on carbon nanotubes: the role of oxygen functional groups, *Environ. Sci. Technol.* 54 (2020) 1267–1275.
- [33] H. Fei, J. Dong, Y. Feng, C.S. Allen, C. Wan, B. Voloskiy, M. Li, Z. Zhao, Y. Wang, H. Sun, P. An, W. Chen, Z. Guo, C. Lee, D. Chen, I. Shaker, M. Liu, T. Hu, Y. Li, A. I. Kirkland, X. Duan, Y. Huang, General synthesis and definitive structural identification of MN₄C₄ single-atom catalysts with tunable electrocatalytic activities, *Nat. Catal.* 1 (2018) 63–72.
- [34] X. Li, X. Huang, S. Xi, S. Miao, J. Ding, W. Cai, S. Liu, X. Yang, H. Yang, J. Gao, J. Wang, Y. Huang, T. Zhang, B. Liu, Single cobalt atoms anchored on porous N-doped graphene with dual reaction sites for efficient fenton-like catalysis, *J. Am. Chem. Soc.* 140 (2018) 12469–12475.
- [35] H. Yang, L. Shang, Q. Zhang, R. Shi, G.I.N. Waterhouse, L. Gu, T. Zhang, A universal ligand mediated method for large scale synthesis of transition metal single atom catalysts, *Nat. Commun.* 10 (2019) 4585.
- [36] H. Wang, Y. Wang, J. Zhang, X. Liu, S. Tao, Electronic structure engineering through Fe-doping CoP enables hydrogen evolution coupled with electro-Fenton, *Nano Energy* 84 (2021).
- [37] K. Yuan, D. Lützenkirchen-Hecht, L. Li, L. Shuai, Y. Li, R. Cao, M. Qiu, X. Zhuang, M.K.H. Leung, Y. Chen, U. Scherf, Boosting oxygen reduction of single iron active sites via geometric and electronic engineering: nitrogen and phosphorus dual coordination, *J. Am. Chem. Soc.* 142 (2020) 2404–2412.
- [38] P. Liang, C. Zhang, X. Duan, H. Sun, S. Liu, M.O. Tade, S. Wang, N-doped graphene from metal-organic frameworks for catalytic oxidation of p-hydroxybenzoic acid: N-functionality and mechanism, *ACS Sustain. Chem. Eng.* 5 (2017) 2693–2701.
- [39] Y. Gao, Y. Zhou, S.Y. Pang, J. Jiang, Y.M. Shen, Y. Song, J.B. Duan, Q. Guo, Enhanced peroxymonosulfate activation via complexed Mn(II): a novel non-radical oxidation mechanism involving manganese intermediates, *Water Res.* 193 (2021), 116856.
- [40] B. Shao, H. Dong, B. Sun, X. Guan, Role of ferrate(IV) and ferrate(V) in activating ferrate(VI) by calcium sulfite for enhanced oxidation of organic contaminants, *Environ. Sci. Technol.* 53 (2019) 894–902.
- [41] H. Zhang, L. Lyu, Q. Fang, C. Hu, S. Zhan, T. Li, Cation- π structure inducing efficient peroxymonosulfate activation for pollutant degradation over atomically dispersed cobalt bonding graphene-like nanospheres, *Appl. Catal. B: Environ.* 286 (2021).
- [42] Z. Wang, N. Goyal, L. Liu, D.C.W. Tsang, J. Shang, W. Liu, G. Li, N-doped porous carbon derived from polypyrrole for CO₂ capture from humid flue gases, *Chem. Eng. J.* 396 (2020).
- [43] G.G. Haciosmanoglu, T. Dogruel, S. Genc, E.T. Oner, Z.S. Can, Adsorptive removal of bisphenol A from aqueous solutions using phosphonated levan, *J. Hazard Mater.* 374 (2019) 43–49.
- [44] K. Yuan, S. Sfaelou, M. Qiu, D. Lützenkirchen-Hecht, X. Zhuang, Y. Chen, C. Yuan, X. Feng, U. Scherf, Synergetic contribution of boron and Fe-N_x species in porous carbons toward efficient electrocatalysts for oxygen reduction reaction, *ACS Energy Lett.* 3 (2017) 252–260.
- [45] D. Xia, X. Yang, L. Xie, Y. Wei, W. Jiang, M. Dou, X. Li, J. Li, L. Gan, F. Kang, Direct growth of carbon nanotubes doped with single atomic Fe-N₄ active sites and neighboring graphitic nitrogen for efficient and stable oxygen reduction electrocatalysis, *Adv. Funct. Mater.* 29 (2019).
- [46] H. Cai, G. Zhang, X. Zhang, B. Chen, Z. Lu, H. Xu, R. Gao, C. Shi, Engineering the local coordination environment and density of FeN₄ sites by Mn cooperation for electrocatalytic oxygen reduction, *Small* 18 (2022), e2200911.
- [47] Y. Liu, J. Luo, L. Tang, C. Feng, J. Wang, Y. Deng, H. Liu, J. Yu, H. Feng, J. Wang, Origin of the enhanced reusability and electron transfer of the carbon-coated Mn₃O₄ nanocube for persulfate activation, *ACS Catal.* 10 (2020) 14857–14870.